

# Computation of Unmeasured 3<sup>rd</sup> Generation VCT Views from Measured Views - Preliminary Results

S. K. Patch

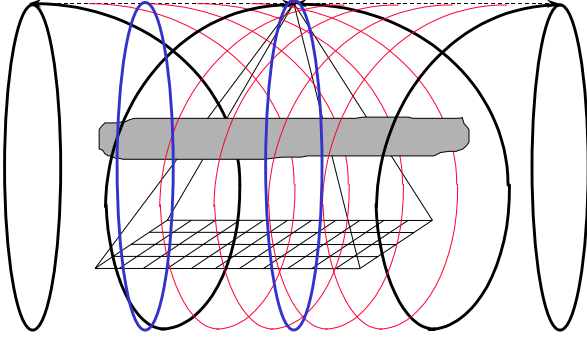


Figure 1. Measured source trajectory shown in black. Axial scans immediately precede and follow a helix, providing mathematically complete data for unbounded objects. Views corresponding to focal spot positions on a neighboring helix, shown in red, are computed at each iteration of our numerical PDE solver. Data corresponding to axial scans shown in blue at  $z = 0$  and  $z = -0.063\text{m}$  were saved to reconstruct in those planes by standard 2D filtered backprojection.

**Abstract—** We generalize work done in [1] by computing unmeasured cone beam projections from measured projections. We do this by solving a characteristic boundary value problem for an ultrahyperbolic differential equation [2]. One potential use for this technique is reduction of cone-angle artifacts suffered by approximate volumetric reconstruction techniques, including Feldkamp. By working in the Fourier domain, we convert the 2<sup>nd</sup> order PDE into a family of 1<sup>st</sup> order ODE's. A simple 1<sup>st</sup> order integration is used to solve the ODEs.

**Keywords—** ultrahyperbolic partial differential equation, cone-beam CT

## I. INTRODUCTION

WE compute unmeasured volumetric computed tomography (VCT) views from measured views by enforcing range conditions [2] requiring that VCT data satisfy the ultrahyperbolic partial differential equations:

$$\left( \frac{\partial^2}{\partial \eta_i \partial \xi_j} - \frac{\partial^2}{\partial \eta_j \partial \xi_i} \right) u(\xi; \eta) = 0 \quad \text{for } i, j = 1, 2, 3 \quad (1)$$

By solving a characteristic boundary value problem for these equations, unmeasured views corresponding to unmeasured axial scans are computed. See Figure 1.

Fritz John's range conditions in equation 1 were published in '38 and the idea of computing unmeasured views

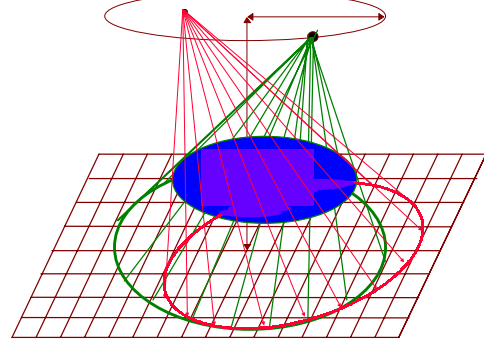


Fig. 2. Source trajectory is a horizontal circle above the patient. Unmeasured cone-beam projections are computed for focal spot positions within the circle

has been considered for tomosynthesis type systems. In [1] Edholm & Danielsson showed that *cone beam* projections measured by a circular source trajectory lying in a single plane could be used to compute *parallel beam* projections of a *different* object. Their derivation uses fundamental geometric arguments, as does the derivation in [3] showing the necessity of John's equation 1 for xray-transforms of smooth, compactly supported functions. The same measured cone beam projections are used to compute *unmeasured cone beam* projections of the *same* object. See Figure 2. The projections are computed in [3] much as we do in this paper, by solving John's equation 1 in the Fourier domain. The tomosynthesis geometry allowed us to solve analytically, whereas the helical system we consider here requires a change of variables which creates a nasty forcing term in the right-hand side of the transformed equation. We have not found an analytical solution, so the results presented here were computed using crude first-order integration.

John first introduced the ultrahyperbolic equation in a different form, equivalent to 1 by a linear change of variables. The original equation's variables did not correspond to the xray transform used in computed tomography, but did permit a mean-value theorem [4] and even analytic solutions for special geometries [5],[6]. A mathematically exact inversion formula exploiting John's equation was presented for "bounded" objects in [7].

Normalized VCT data measures line integrals of a three dimensional imaging object's linear attenuation coefficient (LAC). The 1-dimensional source trajectory along which we measure cone beam projections with a 2-dimensional

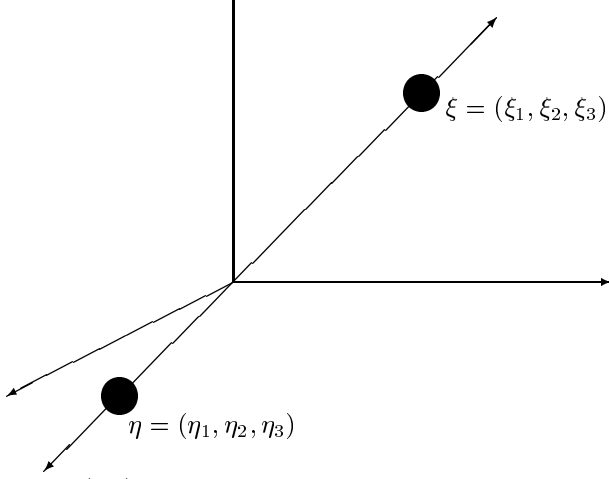


Fig. 3.  $X\rho(\eta; \xi)$  integrates  $\rho$  along the line passing through  $\eta$  and  $\xi$ .

xray detector with pixels parameterized by  $(\alpha_1, \alpha_2)$ , providing  $1 + 2 = 3$  dimensions worth of boundary value (BV) data on a characteristic surface. For a constant-pitch helix of pitch  $p \geq 0$  where the FS moves a distance  $\frac{p}{2\pi}$  during a single rotation, we measure on the  $1 + 2 = 3$  dimensional surface defined by

$$z = p\theta \quad \text{where } \alpha_1, \alpha_2 \text{ are free}$$

We change variables to parameterize  $3^{rd}$ -Gen data and rewrite the consistency conditions in the new coordinate system. Notice that 1 is written in terms of six variables. Figure 3. Our measured data represents line integrals of a function defined in  $R^3$  and therefore should be a function of three independent variables. However, in a  $3^{rd}$ -Gen system, the radii of rotation are fixed so we only measure  $u$  for varying  $\theta$ ,  $z$ ,  $\alpha_1$ , and  $\alpha_2$ , where  $(\theta, z)$  parametrize focal spot (FS) positions and  $(\alpha_1, \alpha_2)$  correspond to pixel location on a flat panel xray detector. See Figure 1. In order for our dimension count to be correct there can be only one *independent* constraint upon  $u$ . Modulo first order identities on  $u$ , all three of the conditions in 1 boil down to the single constraint:

$$\frac{\partial u_{\alpha_2}}{\partial \theta} - \rho \frac{\partial u_{\alpha_1}}{\partial z} = \frac{-1}{(\rho + d)} (2\alpha_1 u_{\alpha_2} + \alpha_1 \alpha_2 u_{\alpha_2, \alpha_2} + [(\rho + d)^2 + \alpha_1^2] u_{\alpha_2, \alpha_1}) \quad (2)$$

subject to the boundary conditions *which we measure*

$$u(\theta, p\theta; \alpha_1, \alpha_2) = f(\theta; \alpha_1, \alpha_2) \quad (3)$$

where  $\rho$  and  $d$  represent source-to-iso and iso-to-detector distances, respectively. Notice that the left hand side of 2 is first order with respect to  $z$  and  $\theta$ . Although standard numerical solvers for partial differential equations (PDEs) can be used to solve 2, it is also possible to transform this single PDE into a coupled system of ordinary differential equations (ODEs), which we solve with a first-order integration. Numerical results are presented in Section II.

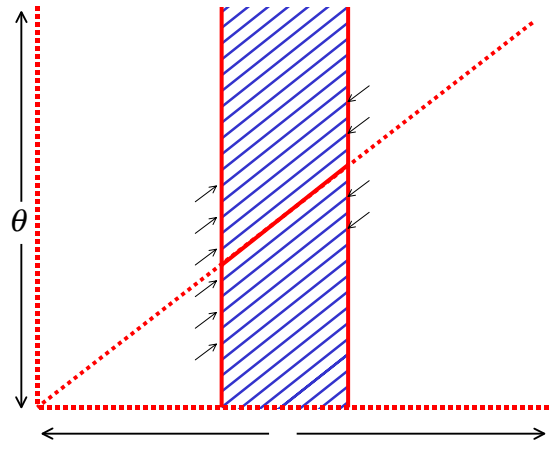


Fig. 4. Source trajectory for results presented here is comprised of circles connected by a short helical segment, shown in bold red. Each iteration of the PDE solver computed views along one of the blue helical segments. Ideally, the helix is longer, but computational costs prohibited us from using a full rotation helix to generate these preliminary results.

## II. NUMERICAL RESULTS

Preliminary results are presented here for a source trajectory failing the Kirillov-Tuy completeness condition. We consider here only data measured on a short segment of a constant pitch helical segment source trajectory. Results are computed both with and without noise in the measured data. The incompleteness of our measured data implies that a wedge of Fourier components comprising less than 2% of the Fourier components of our computed projections are inaccessible. We therefore fill in these missing Fourier data both with and without noise. We hope to extend our numerical solver to handle complete source trajectories consisting of two axial scan trajectories connected by a constant pitch helical scan. (Remember, an axial scan corresponds to pitch  $p = 0$ !)

### A. System Configuration

Noise-free test data of a simple phantom object was simulated assuming a  $512 \times 512$  array with pixel pitch of  $1.5e - 3$  m, source trajectory with helical pitch 150 measured at isocenter, and 984 views per  $2\pi$  gantry rotation. The FS moves on a radius of  $0.541$  m, whereas the detector is slightly closer to the  $z$ -axis, rotating at a distance of  $0.408$  m. With this system geometry and helical pitch, the FS moves  $0.128$  m in a single rotation. Note that we are working nowhere near the theoretical maximum pitch for exact reconstruction. With this (perhaps suboptimal) discretization,  $dz \ll d\theta$  and at each iteration of our PDE solver, only a few neighboring projections contribute to the next step. See Figure 4. In the tests presented here we solved only for projections on a thin ring around the center of our phantom to reduce computation time.

Our phantom object is unbounded, consisting of one large ellipsoid full of water and containing several homo-

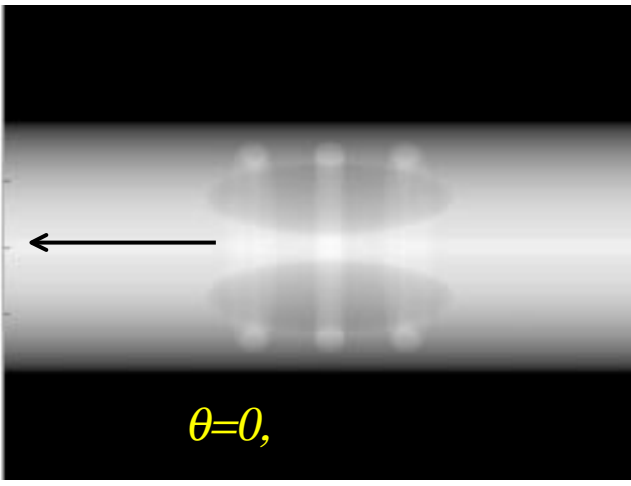


Fig. 5. Projection measured with FS at  $(\theta, z) = (0, 0)$ . The spine parallel to the  $z$ -axis is barely visible.

geneous density inclusions: one thin rod parallel to the patient axis, two smaller ellipsoidal air pockets which are surrounded by three higher density rings. The rod simulates a spine, the air pockets simulate lungs, and the rings simulate ribs. Object centers, dimensions, and densities listed below:

tissue type	center (cm)	eccentricities/radii (cm)	density = LAC
water body	(0, 0, 0)	(20, 10, 1e6)	190
spine	(-4, 0, 0)	(1, 1, 1e6)	304
lung <sub>1</sub>	(2, -4, 0)	(3, 3, 8)	0
lung <sub>2</sub>	(2, 4, 0)	(3, 3, 8)	0
rib <sub>1</sub>	(0, 0, -5)	1/8.5	304
rib <sub>2</sub>	(0, 0, 0)	1/8.5	304
rib <sub>3</sub>	(0, 0, 5)	1/8.5	304

Table 1. Different tissue types, their sizes, positions, and attenuation coefficients are listed above.

The linear attenuation coefficient (LAC),  $u \in C_0$  is bounded and for each  $(\theta, z)$  pair, has compact support in  $\alpha_1$ , and  $\alpha_2$ . However, the LAC is “unbounded” with respect to the detector, since the water body and spine are longer than the detector. We should note that this is a relatively benign with little frequency content in the  $z$ -direction. A projection taken with focal spot in the central plane is shown in Figure 5.

### B. Noise-Free Results

Boundary value data as described in 3 from source positions on the helical source trajectory were first simulated without noise and used to solve equation 2. The central columns from each projection with a full of spot position in the middle blue circle shown in Figure 1 were compiled to create a 2D axial sinogram. The reconstruction of that central plane is compared to the mathematically exact image in Figure 6. Notice the slight shading across the image and broadening of the rib. These errors are due to inaccuracies in our first-order numerical solver, since our data is

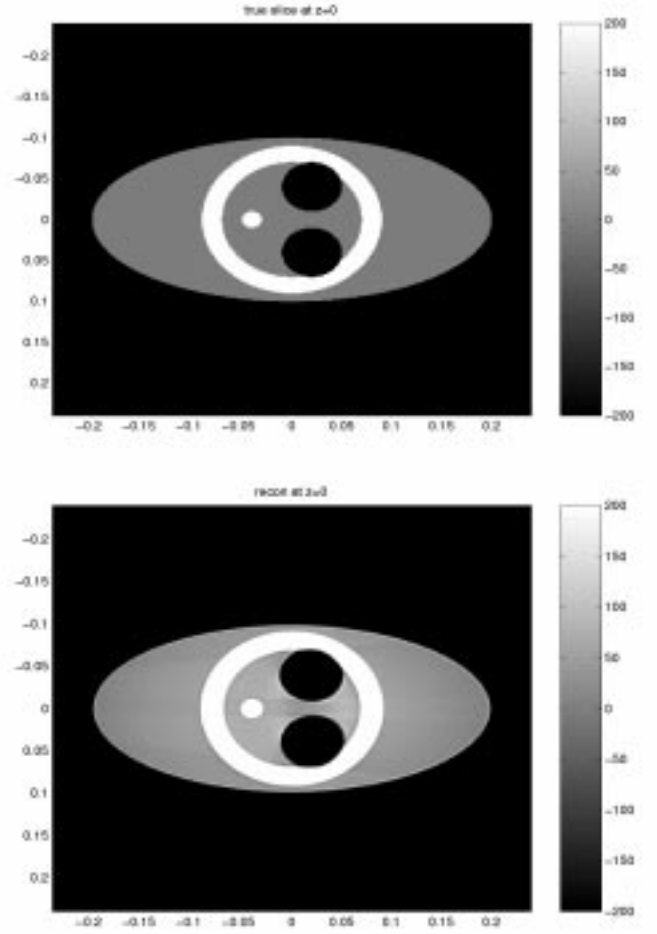


Fig. 6. Reconstruction via standard 2D filtered-backprojection of true and computed sinograms. No noise was added to the projections from which the second sinogram was computed.

noise-free. Vertical and horizontal profiles across this same reconstructed slice are shown in Figure 7.

### C. Noisy Results

The same code was run to test robustness to noise where both additive and multiplicative noise were added to all “measured” projections as follows:

$$u_{noisy}(\theta, \alpha_1, \alpha_2) = u_{true}(\theta, \alpha_1, \alpha_2)(1 + 0.005X) + 0.05Y \quad (4)$$

where  $X, Y \in N(0, 1)$ . Projections in the axial sinogram computed from noisy BV data are compared to noisy sinogram projections with the same noise levels in Figure 8. Whether the differences are repeatable for different realizations of the experiment remains to be determined.

## III. CONCLUSION

For “bounded” objects, 3<sup>rd</sup>-Gen helical VCT data can be reconstructed exactly once the 3<sup>rd</sup>-Gen version of John’s equation has been solved. To reconstruct a volume using

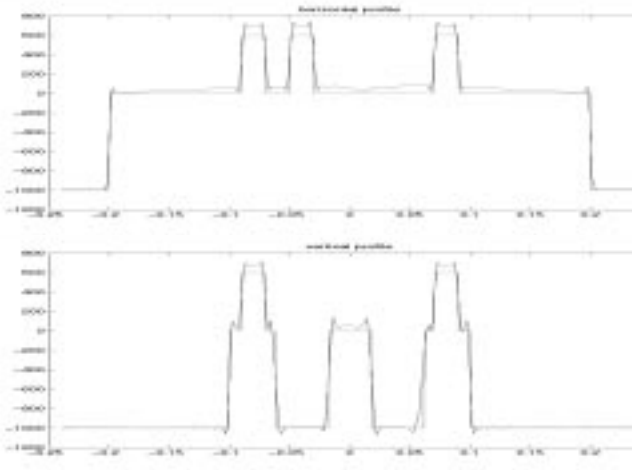


Fig. 7. Notice that Gibbs ringing is the largest source of error in the vertical profile (bottom) but that the shading artifact can be seen in the horizontal profile (top). In both cases, locations of edges are accurately recovered.

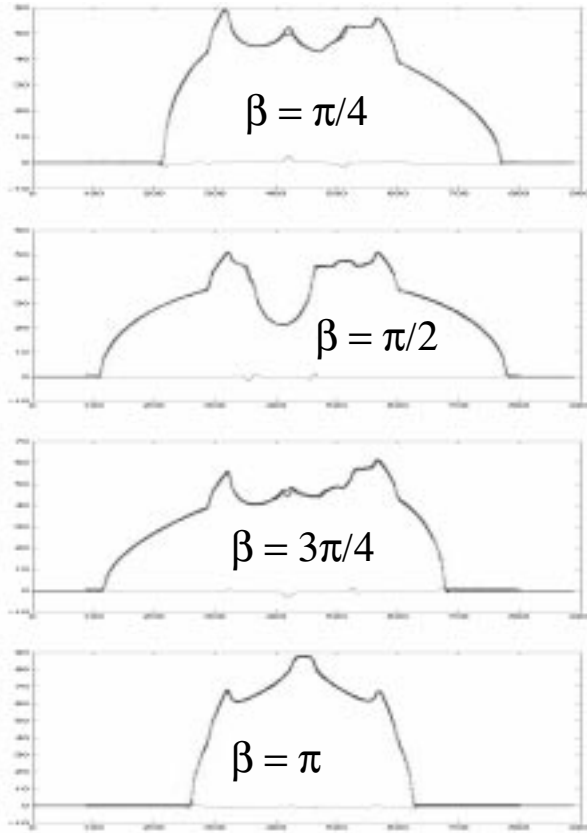


Fig. 8. Profiles of projections computed from noisy boundary value data as well as noisy projections measured directly are both plotted in heavy dots. The difference between these noisy profiles is plotted below in a thin black line.

2D filtered backprojection, we solve for all projections corresponding to focal spot positions on the cylinder, saving at each iteration only data on the central columns to generate 2D axial sinograms. Because our numerical scheme was low order, we were forced to solve for all projections anyway. A higher-order solver would allow us to take larger step sizes, and more importantly, improve our solution accuracy. However, a high-order scheme is elusive [10].

Our next task in this effort is to incorporate boundary value data from 2 circles + helix source trajectory, eliminating the need to “fill in” inaccessible Fourier components. This is straightforward numerical work. Our next task, developing an exact method for “unbounded objects” will require more effort. Views of unbounded objects are not exactly recovered using this technique. Whoever as the size of the flat panel detector rate increases errors due to the unbounded object problem decrease. Although the errors are likely to be small, a mathematically exact solution analogous to that in [8],[9] is required to complete our analysis.

## REFERENCES

- [1] Edholm, P.R., Danielsson, P.E., “A Theorem on Divergent Projections,” *Three Dimensional Image Reconstruction in Radiation and Nuclear Medicine*, P. Grangeat & J.L. Amans, eds., pp. 35-45, (1996).
- [2] John, F., “The Ultrahyperbolic equation with 4 independent variables”, *Duke Math. Journal*, pp. 300-322, (1938).
- [3] Patch, S. K., “Almost-Everywhere Extrapolation using 2D Transforms from Cone Beam Data”, U.S. Patent #6,173,030, (2001).
- [4] Asgierrson, L., “Ueber eine Mittelwertseigenschaft von Loesungen homogener linearer partieller Differentialgleichungen zweiter Ordnung mit konstanten Koeffizienten”, *Mathematische Annalen*, 13, pp. 321-346, (1938).
- [5] Owens, G., “An Explicit formula for the solution of the Ultrahyperbolic Equation in four Variables”, *Duke Math Journal*, 9, pp. 272-282, (1942).
- [6] Owens, G., “A Boundary-Value Problem for Analytic Solutions of an Ultrahyperbolic Equation” *Duke Math Journal*, 20, pp. 29-38, (1953).
- [7] D. Finch, “Cone Beam Reconstruction with Sources on a Curve,” *SIAM J. Appl. Math.*, **45** #4, pp. 665-673, (1985).
- [8] Tam, K., US Patent #5,390,111, “Method and System for Processing Cone Beam Data for Reconstructing Free of Boundary-Induced Artifacts a Three Dimensional Computerized Tomography Image,” 1993.
- [9] Kudo H., Noo, F., Defrise, M., “Cone-beam filtered-backprojection algorithm for truncated helical data,” *Phys. Med. Biol.*, 43, pp. 2885-2909, (1998).
- [10] J. Hu, C. Ingrassia, S. Lowitsch, J. Park, A. Pineda, D. Reynolds, N. Valdivia, *Final Report of the IMA Summer Workshop of Mathematical Modeling in Industry*, July, 2000, posted at [www.ima.umn.edu](http://www.ima.umn.edu).
- [11] Greenleaf, A., Uhlmann, G., “Non-Local Inversion Formulas for the X-ray Transform,” *Duke Mathematical Journal*, **58**, no. 1, pp. 205-240, (1989).
- [12] Kirillov, A.A., “On a Problem of I.M. Gelfand”, *Sov. Doklady*, pp. 268-269.
- [13] Tuy, H.K., “An inversion formula for cone-beam reconstruction,” *SIAM J. Applied Math*, 43, pp. 546-552, (1983).
- [14] Grangeat, P., “Mathematical Framework of cone beam 3D reconstruction via the first derivative of the Radon transform,” *Mathematical Methods in Tomography - Lecture Notes in Mathematics*, pp. 66-97, (1991).
- [15] Helgason, S., *The Radon Transform*, Birkhauser, 1980.
- [16] Natterer, F., *The Mathematics of Computerized Tomography*, Wiley, 1986.